HIGH-RESOLUTION SPECTROSCOPY OF COOL CARBON-RICH AND METAL-POOR STAR HD 209621

E. Matrozis, L. Začs and A. Barzdis

Faculty of Physics and Mathematics, University of Latvia, Raiņa bulvāris 19, LV-1586 Rīga, Latvia; e-mat@inbox.lv, zacs@latnet.lv, arturs-lv@inbox.lv

Received: 2012 February 27; revised May 28; accepted: July 8

Abstract. Element abundances for HD 209621 obtained earlier display significant discrepancies, especially in the case of CNO and neutron-capture elements. Therefore we performed a detailed analysis of chemical composition of this star using a new high-resolution spectrum. Atmospheric parameters and abundance pattern are updated, and the mechanism of nucleosynthesis is examined. Abundances for 11 elements are calculated for the first time. The method of atmospheric models and spectral synthesis was used. The following values of atmospheric parameters are derived: $T_{\rm eff}=4400~{\rm K}, \log~g=1.0~{\rm (cgs)}$ and $\xi_t=1.9~{\rm km\,s^{-1}}$. The iron abundance of the star was found to be low, at [Fe/H] = -1.91 ± 0.10. The carbon to oxygen ratio is high, C/O \simeq +2.0. Low carbon to nitrogen ratio, [C/N] \simeq -0.8, and low carbon isotopic ratio, $^{12}{\rm C}/^{13}{\rm C}=17$ ±5, are in agreement with the theory of nucleosynthesis of intermediate-mass AGB stars. The barium to europium ratio is high, [Ba/Eu] = +0.28, and is typical for carbon-enhanced metal-poor CEMP-r/s stars. The observed abundance pattern of neutron capture elements is reproduced well by the scaled solar system abundances.

Key words: stars: abundances, atmospheres, spectroscopic binaries, carbon, individual: HD 209621

1. INTRODUCTION

CH stars are metal-poor red giants with enhanced abundances of carbon and s-process elements. Lines of CH molecule and heavy elements, such as strontium and barium, are very strong in the spectra of these halo stars (Keenan & Morgan 1941). Abundance pattern of metal-poor stars gives unique information about the nucleosynthesis of the first generation stars and early enrichment in the Galactic halo. Detailed examinations of chemical and isotopic anomalies encourage improvements in the theory of nucleosynthesis and convection. Most of the stars classified as CH stars seem to be Population II counterparts of barium stars – long period binaries with invisible (white dwarf) companion in the optical region (McClure & Woodsworth 1990). The observed abundance anomalies are explained by mass transfer from the former asymptotic giant branch (AGB) star to the companion of lower initial mass (Han et al. 1995). Although all bright CH stars have been analyzed before, using methods of high-resolution spectroscopy, the updates are still important. Sometimes the abundances calculated by different authors display

significant discrepancies, especially for the CNO and neutron-capture elements.

HD 209621 is a high latitude ($b=-27^{\circ}$), 8.9 magnitude star in the visual region classified before as R3 and C1,2 CH (Keenan & Morgan 1941; Yamashita 1975). Irregular brightness variations (Lb) are observed with an amplitude of about 0.1 mag in the photographic band (Samus 2007). For HD 209621 Sanford (1924) measured a high radial velocity, $-382.6~{\rm km\,s^{-1}}$. Twenty seven radial velocity data, monitored by McClure & Woodsworth (1990) in the time span of more than 6 years, revealed regular velocity variations with an amplitude of about 25 km s⁻¹ and a period of 407.4 \pm 1.1 days. Circularized orbit and low mass function was calculated for this binary, f(m) = 0.074 M_{\odot} . Its parallax value is rather uncertain, $\pi=1.47\pm1.30$ mas (Perryman et al. 1997). Bolometric magnitude was estimated by Bergeat, Knapik & Rutily (2002), $M_{\rm bol}=-1.9$ mag. The basic data for HD 209621, available in the literature, are summarized in Table 1.

Atmospheric parameters and abundances for HD 209621 have been calculated before, using the methods of high-resolution spectroscopy and atmospheric models by Wallerstein (1969), Tsuji et al. (1991), Vanture (1992a,b) and Goswami & Aoki (2010). The effective temperature was found to be in the range from about 4200 to 4700 K on the basis of color indices and the excitation analysis of iron lines. Ionization balance for iron lines provides the surface gravity $\log q$ of about 2.0 (cgs). The microturbulent velocity was found to be between 2 and 3 km s⁻¹. HD 209621 is clearly metal-poor and rich in s-process elements. However, the estimates of metallicity are contradictory, [Fe/H] was found to be from -0.9 dex (Vanture 1992b) to −1.9 dex (Goswami & Aoki 2010), and a significant discrepancy was detected for the most of neutron-capture elements up to 0.7 dex in [X/Fe] for yttrium and cerium. Unfortunately, most of the abundances calculated in the recent paper published by Goswami & Aoki (2010) were based only on single lines, and the real uncertainties are not known. The carbon abundance ranges from $\log \epsilon(C) = 7.7$ (Goswami & Aoki 2010) to 8.5 (Vanture 1992a). The nitrogen abundance calculated using CN lines is $\log \epsilon(N) = 8.2$ (Vanture 1992b). The estimate of the carbon and nitrogen abundances is coupled, therefore the uncertainty in the nitrogen abundance is unknown. Spectroscopic estimates of the oxygen abundance for HD 209621 are absent. Spectral synthesis of selected C₂ and CN lines provides a low carbon isotopic ratio of ¹²C/¹³C from 3.5 (Vanture 1992a) to 11.2 (Tsuji et al. 1991).

Results of the detailed abundance analysis are presented here, using the methods of high-resolution spectroscopy and atmospheric models. The atmospheric parameters and abundances for 32 elements are updated, or calculated for the first time (for 11 elements). The gravity calculated/adopted in previous papers was found to be overestimated. Four independent arguments are provided in support of lower gravity, $\log g = 1.0$ (cgs). The abundances for eight neutron-capture elements are calculated using at least three lines, and the standard deviations are derived. Confrontation of the abundance pattern with standard solar system abundances is provided, and the mechanism of nucleosynthesis is updated.

2. OBSERVATIONS AND DATA REDUCTION

A high resolution spectrum of HD 209621 was obtained on 2008 August 24 with the FIbre-fed Echelle Spectrograph (FIES) on the 2.5 m Nordic Optical Telescope (NOT) at La Palma, with resolving power of $R=67\,000$. The spectrum covers the wavelength region from about 3650 to 7350 Å with a signal-to-noise

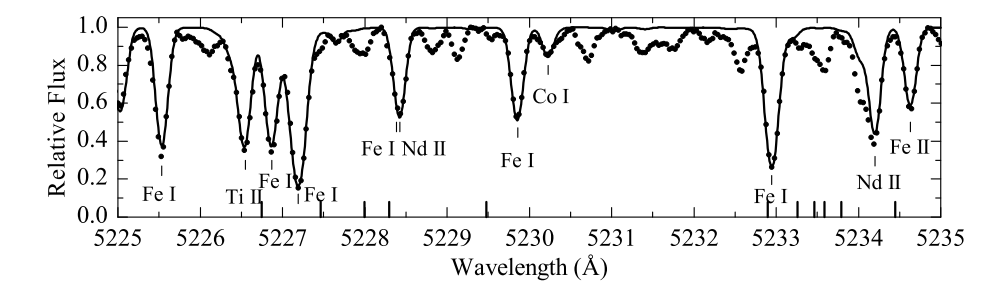


Fig. 1. Observed spectrum of HD 209621 (dots) in the wavelength region less affected by molecular features. The important lines are identified by their chemical symbol. The synthetic spectrum is given for selected lines, calculated using the final atmospheric parameters and abundances.

Table 1. Basic data for HD 209621, available in literature.

V	B– V	E_{B-V}	$T_{\mathrm{eff}}\left(\mathbf{K}\right)$	$\log g$	$\xi_t \; (\mathrm{km}\mathrm{s}^{-1})$	[Fe/H]	Ref.
0	1.45 1.47	0.10	4700	-	-	-1.3	1
-	-	0.08	$4400 \\ 4700$	$\frac{2.0}{1.8}$	$\frac{3.0}{2.0}$	-0.90	$\frac{2}{3}$
- 8.89	-1.45	_	4190	_	_ _	— —	4 5
-	- 1 45	-	4500	2.0	2.0	-1.93	6
- 8.89 - 8.89	- 1.45 - 1.45	- - - 0.20	=	- 2.0 1.0	2.0 1.9	- -1.93 -1.91	

References: 1 – Wallerstein (1969), 2 – Tsuji et al. (1991), 3 – Vanture (1992b), 4 – Bergeat et al. (2002), 5 – Platais et al.(2003), 6 – Goswami & Aoki (2010), 7 – this work.

ratio ~ 100 . The reduction of CCD frames (subtraction of bias, dark and scattered light, flat-fielding, extraction of echelle orders and wavelength calibration) was performed with the data reduction software FIEStool¹. Normalization of the spectrum and measurements of equivalent widths were made using the DECH software² (Galazutdinov 1992). An extract from a normalized spectrum of HD 209621 is shown in Figure 1.

3. ANALYSIS AND RESULTS

3.1. Line selection and measurements

Inspection of the spectrum of HD 209621 shows that lines of the iron-peak elements are weak, while lines of C_2 , CN and the neutron-capture elements are enhanced relative to a medium metal-poor giant Arcturus (G8 IIIab) of similar effective temperature and gravity. The crowded spectrum and continuum definition is a serious problem – atomic lines in several regions are significantly blended with the molecular bands. Unblended atomic lines are selected in wavelength regions less affected by molecular features, using atomic and molecular line lists. The

¹ http://www.not.iac.es/instruments/fies/fiestool/FIEStool.html

 $^{^2}$ http://www.gazinur.com/Download.html

measurements of equivalent widths are performed by fitting the line profiles with the Gaussian.

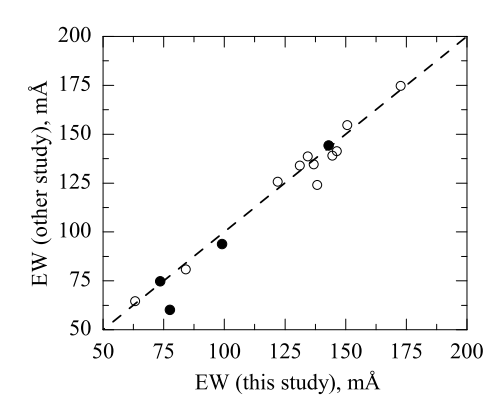


Fig. 2. Comparison of the equivalent widths of Fe I (\circ) and Fe II (\bullet) lines in HD 209621 measured in this study and by Goswami & Aoki (2010).

In Table 2 we give the equivalent widths (EW) for all lines used for abundance calculations, along with the oscillator strengths ($\log gf$) and excitation potentials (LEP). In Figure 2 the comparison of the EWs measured in this study with those measured by Goswami & Aoki (2010) is given. Systematic errors in equivalent widths are absent and the random errors are small for most of the lines, except the EWs measured for Fe I line at 5192.344 Å and Fe II line at 4508.288 Å. The Fe I line is a little blended in the right wing and the Fe II line is slightly asymmetrical. These two lines, along with some other lines with larger uncertainty of measured EWs are marked by (:) in Table 2. However, cancellation of the marked lines changes the calculated mean abundances fractionally.

The standard LTE line analysis program ABUNDANCE, which is a part of spectra synthesis package called SPECTRUM³ written by Gray & Corbally (1994), was applied for calculations of abundances using the equivalent widths. Lines stronger than 200 mÅ as a rule are not used for abundance calculations, except of a few strong barium and sodium lines. Model atmospheres were extracted from the grid of ATLAS models calculated by Castelli & Kurucz (2003). The available atomic data were used together with SPECTRUM and were inspected/updated using the Vienna Atomic Line Database (VALD; Kupka et al. 1999). The adopted atomic data are given in Table 2. Line list, compiled by Zamora et al. (2009) is used for the C₂ and CN lines. In the case of rare-earths, oscillator strengths are examined using the Database of Rare-Earths at Mons University (DREAM; Biémont, Palmeri & Quinet 1999). Profiles of selected atomic and molecular lines were synthesized using the codes STARSP (Tsymbal 1996) and SPECTRUM.

3.2. Radial velocity

The radial velocity for HD 209621 was measured using a number of weak symmetrical absorption lines in the observed (JD 2454698.65) spectrum. Direct and mirror profile of each line was correlated, and the corresponding radial velocity was calculated from a relative shift of the line center from its rest wavelength. The observed velocity was corrected onto the heliocentric system by adding +5.6 km s⁻¹. The mean heliocentric radial velocity RV_{\odot} was found to be -372.3 ± 0.4 km s⁻¹. This value is within the radial velocity range observed for HD 209621 by McClure & Woodsworth (1990).

³ http://www1.appstate.edu/dept/physics/spectrum/spectrum.html

Table 2. Wavelengths, excitation potentials, oscillator strengths and equivalent widths of the lines used for abundance calculations in the spectrum of HD 209621. The lines calculated using the method of spectral synthesis are marked by s .

λ	LEP	$\log gf$	EW	λ	LEP	$\log gf$	EW	λ	LEP	$\log gf$	$\mathbf{E}\mathbf{W}$
(Å)	(eV)		(mÅ)	(Å)	(eV)		(mÅ)	(Å)	(eV)		(mÅ)
Li I				VII				5234.63^{s}	3.22	-2.180	73.5
6707.76^{s}	0	-0.009	62.0	4023.39	1.80	-0.480	55.2	5264.81	3.23	-3.130	27.7
6707.91^{s}	0	-0.309	-	Cr I	1.00	0.400	00.2	5276.00^{s}	3.20	-2.010	91:
Na I	O	0.000		4591.39	0.97	-1.740	48.5	5316.62^{s}	3.15	-1.870	102.9
5682.63^{s}	2.10	-0.700	49.0	5206.04	0.94	0.060	167.1	5362.87	3.20	-2.570	65:
5688.21^{s}	2.10 2.10	-0.760 -0.450	63.5	5200.04 5247.57^{s}	0.94	-1.640	69.0	Co I	5.20	-2.570	05.
5889.95^{s}	0	0.108	366.8	5329.14	2.91	-0.064		3995.30	0.92	-0.220	153.6
5895.92^{s}	0	-0.194	336.2	5329.14 5348.32^{s}	1.00	-0.004 -1.290	84.1		3.22	0.050	36.5
Mg I	U	-0.194	330.2	0346.32 Cr II	1.00	-1.290	04.1	5230.20^{s}	$\frac{3.22}{1.74}$	-1.840	28.9
	2.71	-0.870		4848.24	3.86	-1.280	51.1	5230.20 5331.45^{s}	1.74 1.79		28.7
5167.32^{s}			2400							-1.960	
5172.68^{s}	2.71	-0.393	348.8	4864.33	3.86	-1.470	33.6	5344.56	4.03	0.097	5.6
5183.60^{s}	2.72	-0.167	383.4	4876.40	3.85	-1.580	52.3	5369.59^{s}	1.74	-1.650	34.3
AlI	0.14	1.045	10.0	MnI	0.00	0.000	06.0	Ni I	9.40	0.070	40.0
6696.02^{s}	3.14	-1.347	18.6	4754.04 ^s	2.28	-0.086	86.3		3.48	-0.270	49.3
SiI		0.040		4765.85	2.94	-0.080	44.2		3.54	-0.330	46.0
6142.48^{s}	5.62	-0.919	_	4766.42^{s}	2.92	0.100	62.6	4866.26^{s}	3.54	-0.210	49.0
CaI				5432.55	0	-3.795	69.9	4918.36	3.84	-0.240	33.3
4318.65	1.90	-0.295	112.5	Fe I				4976.32^{s}	1.68	-3.100	23.1
5349.47	2.71	-0.310	66.9	4233.60	2.48	-0.604	127.1	6914.56	1.95	-2.270	62.0
5588.75^{s}	2.53	0.358	118.3	4250.79	1.56	-0.714	205:	Cu I			
5590.11^{s}	2.52	-0.571	69.0	4592.65	1.56	-2.449	119.0	5218.20^{s}	3.82	0.264	_
5594.46^{s}	2.52	0.097	120.8	4903.31	2.88	-0.926	108.9	$\operatorname{Zn} \operatorname{I}$			
6102.72^{s}	1.88	-0.793	115.2	5001.86	3.88	0.010	84.1	4810.53^{s}	4.08	-0.137	64.2
6169.56	2.53	-0.478	94.6	5171.60^{s}	1.49	-1.793	172.7	$\operatorname{Sr} \operatorname{I}$			
$\operatorname{Sc}\operatorname{II}$				5192.34	3.00	-0.421	138:	4607.33^{s}	0	-0.570	98.1
4431.37	0.61	-1.969	74.7	5198.71^{s}	2.22	-2.135	97.8	YII			
5657.90^{s}	1.51	-0.603	112.5	5215.18^{s}	3.27	-0.871	89:	4235.73	0.13	-1.500	91.3
5684.20^{s}	1.51	-1.074	77.4		1.61	-2.150		4982.13^{s}	1.03	-1.290	61.2
6279.74	1.50	-1.265	70.8	5217.92	3.64	-1.719	26.1	5200.41^{s}	0.99	-0.570	95.6
Ti I				5225.53^{s}	0.11	-4.789	118.7	5205.72^{s}	1.03	-0.340	105.1
3998.64	0.05	-0.056	126.5	5229.85^{s}	3.28	-0.967	85.0	6127.48^{s}	0.15	-1.060	21.4
4295.75	0.81	-0.450	75.5	5232.94^{s}	2.94	-0.058	150.6	${ m ZrII}$			
4533.24	0.85	0.476	130.0	5242.49	3.63	-0.967	63.2	3998.97^{s}	0.56	-0.520	82.5
4617.27	1.75	0.389	66.9	5266.56^{s}	3.00	-0.386	134.4	4050.33^{s}	0.71	-1.060	78.8
4991.07^{s}	0.84	0.38	140.2	5307.36	1.61	-2.987	98.2	Mo I			
5022.87^{s}	0.83	-0.434	98.9	5324.18^{s}	3.21	-0.103	144.5	5689.15^{s}	1.38	-1.002	34.2
5024.84^{s}	0.82	-0.602	82.8	5415.20	4.39	0.642	89:	BaII			
5036.46^{s}	1.44	0.13	86.9	5429.70	0.96	-1.879	219:	3891.78	2.51	0.280	80.7
5173.74^{s}	0	-1.118	120.1	5434.52	1.01	-2.122	206:	5853.67^{s}	0.60	-1.000	238.6
5210.39^{s}	0.05	-0.884	133.0	5586.76	3.37	-0.120	122.0	6141.71^{s}	0.70	-0.076	354.2
Ti II				6151.62	2.18	-3.299	47:	6496.93	0.60	-0.377	385.5
3987.61	0.61	-2.930	72.5	7022.95	4.19	-1.250		La II			
4053.82	1.89	-1.130	80.9	FeII	-			4716.44^{s}	0.77	-1.126	78.6
4762.78	1.08	-2.740	75.2	4491.41	2.86	-2.710	59:	4748.73^{s}	0.93	-0.540	79.1
4865.61^{s}	1.12	-2.790	72.3		2.86	-2.440	78:	5303.53^{s}	0.32	-1.350	100.5
VI		,00		4555.89	2.83	-2.400	76.4		-		
5627.63	1.08	-0.363	22.6	4583.84	2.81	-1.930	99.0	3912.42	0.30	-0.340	69.5
6216.36^{s}	0.28	-1.290	21.0	4923.93^{s}	2.89	-1.260		4014.90	0.53	0.140	87.6
0210.00	0.20	1.230	21.0	1020.00	2.03	1.200	140.0	1014.00	0.00	0.140	01.0

Table 2. Continued

λ (Å)	LEP (eV)	$\log gf$	EW (mÅ)	λ (Å)	LEP (eV)	$\log gf$	EW (mÅ)	λ (Å)	LEP (eV)	$\log gf$	EW (mÅ)
4117.29	0.74	-0.525	40.2	4594.45	0.20	-1.360	63.3	4913.26	0.66	-0.930	62.8
4222.60	0.12	0.020	114.2	4786.11	0.18	-1.410	74.2	4972.17^{s}	0.93	-0.929	30.4
4257.12	0.46	-0.850	58.7	4859.03	0.32	-0.440		EuII			
4882.46^{s}	1.53	0.290	61.0	4947.02^{s}	0.56	-1.130	56.3	6437.64^{s}	1.32	-0.320	51.8
4943.44^{s}	1.21	-0.360	42.5	4970.92^{s}	0.32	-1.300	70.3	$\operatorname{Gd} \operatorname{II}$			
5330.56^{s}	0.87	-0.460	72.1	5200.12	0.56	-0.522	87.0	4037.33^{s}	0.65	-0.087	_
$\Pr{ ext{II}}$				5249.58^{s}	0.98	0.200	105.1	4037.89^{s}	0.55	-0.493	_
5219.05^{s}	0.80	-0.150	70.4	5319.82^{s}	0.55	-0.170	117.1	4478.80^{s}	0.59	-1.115	_
5220.11^{s}	0.80	0.320	101.1	5421.55^{s}	0.38	-1.219	70.6	Dy II			
5259.73^{s}	0.63	0.190	101.3	5688.52	0.99	-0.310	88.5	3983.65^{s}	0.54	-0.252	66.4
5292.62^{s}	0.65	-0.280	77.8	$\mathrm{Sm}\mathrm{II}$				3996.69^{s}	0.59	-0.207	66.2
NdII				4220.66	0.54	-0.838	56.7	YbI			
4012.70	0	-0.600	80.5	4318.93^{s}	0.28	-0.250	93.2	3987.99^{s}	0	-0.195	_
4023.00^{s}	0.20	0.040	98.1	4791.58^s	0.10	-1.650	50.2				

3.3. Atmospheric parameters

An excitation analysis of selected unblended iron lines was applied to obtain color-independent estimate of the temperature for HD 209621. The plot of individual line abundances vs. lower excitation potentials (LEP), presented in Figure 3 (right panel), illustrates the procedure of estimate of spectroscopic (excitation) temperature. Zero slope corresponds to the temperature of $T_{\rm eff}=4400~{\rm K}$ for HD 209621. This value agrees well with the effective temperatures estimated by Tsuji et al. (1991) and Goswami & Aoki (2010).

The temperature is estimated using the color indices given by Platais et al. (2003) and Skrutskie et al. (2006), and the mean value of interstellar extinction E_{B-V} (Table 1). Using the empirical calibrations of $T_{\rm eff}$ versus color indices and the metallicity of a star, developed by Alonso et al. (1999), we get $T_{\rm eff}=4091$ K and $T_{\rm eff}=4228$ K for B-V and V-K color indices respectively. However, interstellar components (IS) of sodium D1 and D2 lines are very strong in the spectrum of HD 209621, and the interstellar extinction was suspected to be larger than that given in the literature. The equivalent width of about 400 mÅ for Na I D1 IS line leads to $E_{B-V}\approx 0.20$ mag, according to the calibration provided by Munari & Zwitter (1997). The resulting color temperature for HD 209621, $T_{\rm eff}\approx 4300$ K, in this case is larger than that previously estimated from color indexes. However, for the abundance calculationswe preferred the excitation temperature, because color indices in the spectra of cool peculiar stars can be affected by molecular bands, and color temperatures retrieved with the standard calibrations can be uncertain.

Surface gravity was determined from ionization balance by requiring that neutral and ionized iron lines should provide the same iron abundance (Figure 3). Calculating the abundance of iron for various values of $\log g$ gives $\log g \approx 0$ for $T_{\rm eff} = 4250$ K and $\log g \approx 1.4$ for $T_{\rm eff} = 4500$ K. From the ionization balance, $\log g = 0.9 \pm 0.3$ (cgs) for HD 209621. The gravity estimated by us is much lower than that found by Tsuji et al. (1991) and Goswami & Aoki (2010). Therefore in addition, the actual value of gravity was examined using other methods.

An independent determination of the surface gravity can be made using the well

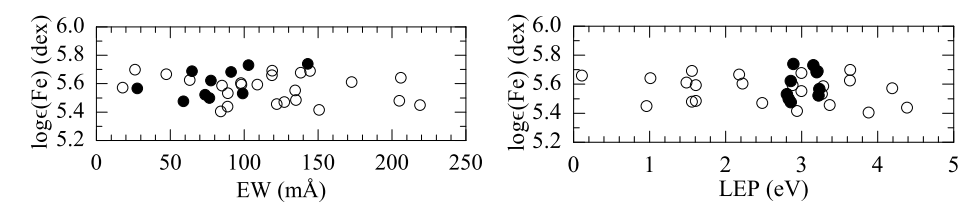


Fig. 3. Plot of the derived abundances from Fe I (o) and Fe II (\bullet) lines vs. the equivalent widths and the lower excitation potentials of these lines calculated for $\xi_t = 1.9 \text{ km s}^{-1}$ and $T_{\rm eff} = 4400 \text{ K}$.

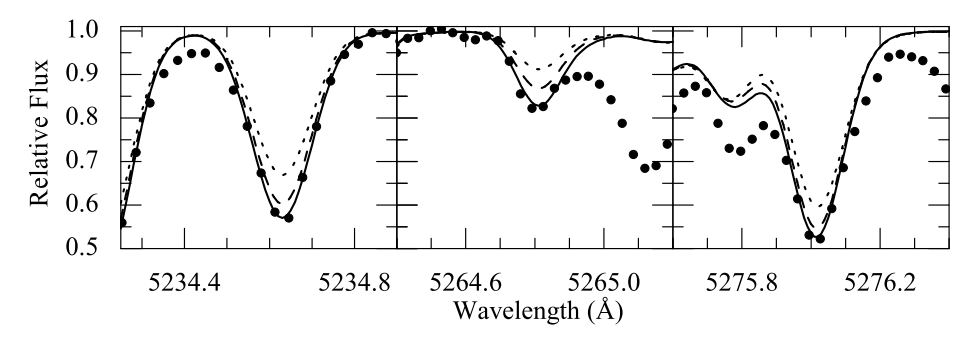


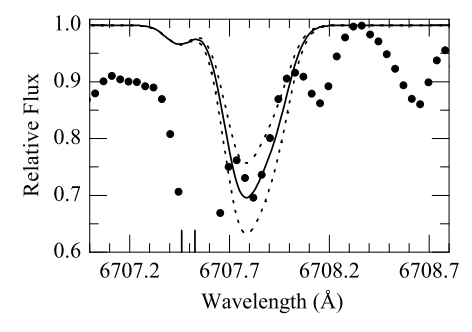
Fig. 4. Three Fe II lines in the spectrum of HD 209621 indicated by dots. The synthetic spectra shown are calculated using the final temperature and the iron abundance $\log \epsilon$ (Fe) = 5.59 for the three gravities: $\log g = 1.0$ (solid line), $\log g = 1.5$ (dashed line) and $\log g = 2.0$ (dotted line).

known relation $\log g = 4 \log T_{\rm eff} + \log M/M_{\odot} + 0.4 M_{\rm bol} - 12.51$, if the bolometric magnitude of the star is known. Using $M_{\rm bol} = -1.9$ mag, $T_{\rm eff} = 4400$ K and adopting a mass of M = 0.8 M_{\odot} typical for CH-stars (McClure & Woodsworth 1990), the relation leads to $\log g \simeq 1.2$ (cgs).

Figure 4 illustrates the synthetic profiles for three unblended Fe II lines used in the abundance calculations. The synthetic spectra calculated for $\log g = 1.0$ (solid line), $\log g = 1.5$ (dashed line) and $\log g = 2.0$ (dotted line) are given. The iron line at 5264.8 Å is most sensitive to variations in surface gravity. The synthetic profile, calculated using $\log g = 1.0$, shows the best fit with the observed one, and it was accepted for abundance calculations in this paper. $\log g$ around 1.0 (cgs) is a typical surface gravity expected for metal-poor giants with the effective temperature around 4400 K (see Figure 1 given by Aoki et al. 2007).

The microturbulent velocity for HD 209621 was estimated by forcing the abundances of the individual iron lines to be independent of the equivalent widths. Twenty four unblended Fe I lines along with ten Fe II lines provided the microturbulent velocity of $\xi_t = 1.9~{\rm km\,s^{-1}}$ (Figure 3, left panel). This value agrees well with the value calculated by Vanture (1992) and Goswami & Aoki (2010).

The atmospheric parameters adopted for the abundance calculations of the star are as follows: $T_{\rm eff} = 4400~{\rm K}$, $\log g = 1.0~({\rm cgs})$ and $\xi_t = 1.9~{\rm km\,s^{-1}}$. Uncertainties in the adopted atmospheric parameters were estimated to be $\pm\,100~{\rm K}$ in temperature, $\pm\,0.3~{\rm dex}$ in gravity and $\pm\,0.3~{\rm km\,s^{-1}}$ in microturbulent velocity.



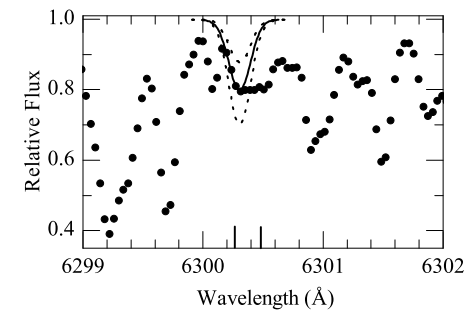


Fig. 5. The observed spectrum of HD 209621 around the lithium feature. The three synthetic spectra shown are given for the lithium abundances $\log \epsilon(\text{Li}) = 1.19 \pm 0.15$. The positions of close CN lines are marked by vertical ticks.

Fig. 6. The observed spectrum of HD 209621 around the forbidden oxygen line at 6300.304 Å. The three synthetic profiles are given for the oxygen abundance $\log \epsilon(O) = 7.54 \pm 0.3$. Positions of the close CN lines are marked by vertical ticks.

3.4. Abundances

Abundances are calculated using the accepted atmospheric parameters and equivalent widths given in Table 2 for the chemical elements, which are represented by unblended or slightly blended lines in the observed spectrum. In addition, selected profiles of atomic lines and several spectral regions with molecular features are calculated using the method of spectral synthesis. The mean absolute and relative abundances in the scale of $\log \epsilon(\mathrm{H}) = 12.0$ derived with $T_{\mathrm{eff}} = 4400$ K, $\log g = 1.0$, $\xi_t = 1.9$ km s⁻¹ and the model metallicity of [M/H] = -2.0 are given in Table 3, together with the standard deviations of abundances (σ) estimated from individual lines, and the number of lines (n) used in the analysis. The abundances relative to the Sun ([X/H]) are calculated using the Solar chemical composition provided by Asplund et al. (2009) for the solar photosphere. Also, the abundances [X/Fe] obtained by Vanture (1992b) and Goswami & Aoki (2010) are given for comparison. Figure 1 illustrates synthesis of selected atomic lines in the wavelength region less affected by molecular features, using the abundances listed in Table 3.

3.4.1. Lithium

The abundance of lithium was estimated using the feature at 6707 Å. Left wing of the profile is blended by CN lines, however, using the method of spectral synthesis, a crude estimation of the lithium abundance is possible. The synthetic profile is very sensitive to variations in the lithium abundance, and leads to the value of $\log \epsilon(\text{Li}) \simeq 1.2$, illustrated in Figure 5. Our estimate agrees with theoretical predictions, confirming a substantial lithium depletion in red giants by surface convection and/or mass accretion from the evolved companion star.

3.4.2. CNO elements

The oxygen abundance was estimated using the forbidden line at 6300 Å. The right wing of the profile is blended by CN, and another CN line is seen on the left wing (Figure 6). However, the contribution of these lines in the core of oxygen line is suspected to be low. According to the VALD database, three more atomic lines are located within the profile of the oxygen line, Cr I, Ni I and Mn II,

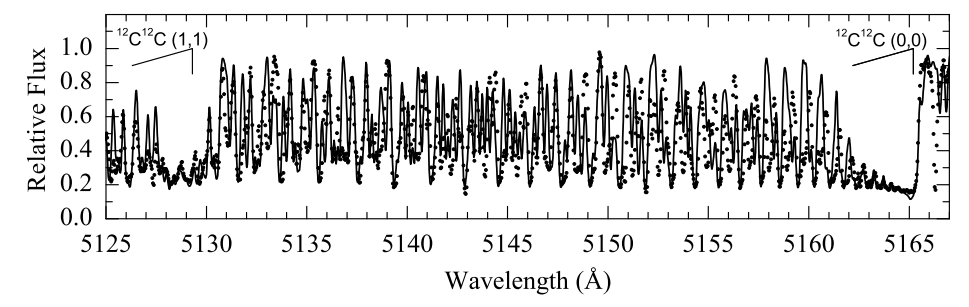


Fig. 7. The observed spectrum of HD 209621 in the wavelength range dominated by the C_2 Swan system (0,0) and (1,1) lines. The synthetic C_2 spectrum is given for the carbon abundance $\log \epsilon(C) = 7.85$.

however, the contribution of these lines is negligible. The contribution of the Sc II line at 6300.7 Å on the right wing of the oxygen line is low because of a good resolution. Spectral synthesis using $\log gf$ values for OI (-9.717) and Ni I (-2.31) lines provided by Prieto et al. (2001) leads to the oxygen abundance of $\log \epsilon(O) \simeq 7.5 \pm 0.2$.

Two spectral regions around the bandheads of C_2 Swan system (0,0), (0,1), (1,1) and (1,2) are synthesized to determine the carbon abundance (Figures 7–9). The line lists compiled by Zamora et al. (2009) have been used. The carbon abundance of $\log \epsilon(C) = 7.85$ resulted as the best fit within uncertainty of 0.1 dex in both spectral regions. The C_2 (1,0) isotopic bandheads at 4737 and 4744 Å are synthesized to derive the $^{12}C/^{13}C$ ratio (Figure 10). Three synthetic spectra calculated for $\log \epsilon(C) = 7.85$ and $^{12}C/^{13}C = 8$, 17 and 20 provide the best fit for the isotopic ratio of 17 ± 5 . This value is slightly larger than the ratios found before. Unfortunately, the use of CN isotopic lines to calculate isotopic ratio was problematic because of absence of the spectrum longward of 7350 Å.

The nitrogen abundance, determined by spectral synthesis of CN Red system lines in the spectral region from about 7190 to 7330 Å, is $\log \epsilon(N) = 8.00 \pm 0.3$. The uncertainty in fitting the synthetic spectrum to the observed one is larger in this case because of lower sensitivity of CN lines to variations of the nitrogen abundance. An extract of the spectrum illustrating synthesis of CN lines is shown in Figure 11.

3.4.3. Odd-Z elements Na, Al and Sc

The resonance doublet D1, D2 and the lines at 5682.63 and 5688.21 Å, arising from the 3^2P-4^2D transition, are selected for the abundance analysis of sodium. Spectral synthesis of the lines at 5682/5688 Å provide the sodium abundance of $\log \epsilon(\mathrm{Na}) = 4.90$ (Figure 12). The resonance lines are less sensitive to variations in the sodium abundance, and the last should be about 0.3 dex larger to reproduce the D1, D2 profiles. However, the non-LTE (NLTE) effects for D1, D2 lines are significant and non-LTE corrections are up to -0.4 dex, according Aoki et al. (2007). Thus, sodium is enhanced in the atmosphere of HD 209621 up to [Na/Fe] = +0.57.

The abundance of aluminum was found to be $\log \epsilon(Al) = 5.18$ using EW of the AlI line at 6696.0 Å. Reasonably good fit of the profile is obtained with $\log \epsilon(Al) = 5.04$ using the method of spectral synthesis. Thus, overabundance

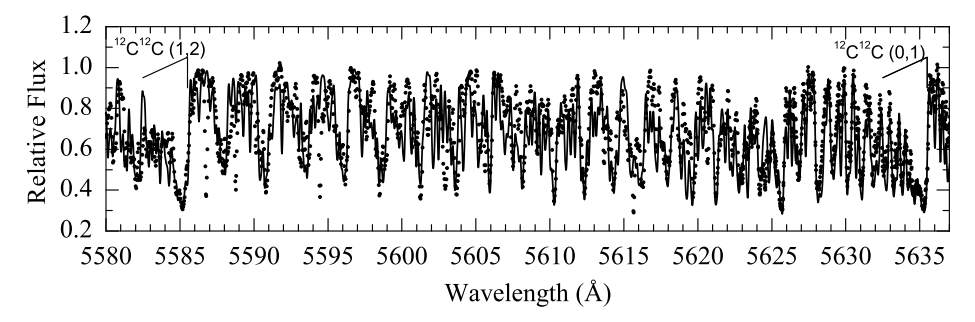


Fig. 8. The observed spectrum of HD 209621 in the wavelength range dominated by the C_2 Swan system (0,1) and (1,2) lines. The synthetic C_2 spectrum is given for the carbon abundance $\log \epsilon(C) = 7.85$.

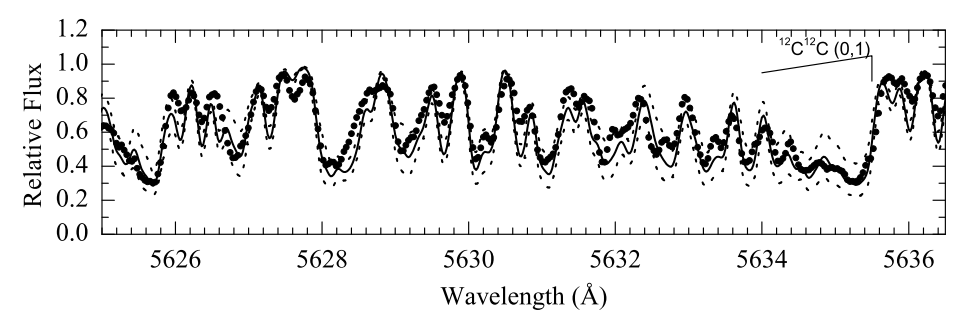


Fig. 9. The observed spectrum of HD 209621 in the wavelength range dominated by the C_2 Swan system (0,1) lines. The synthetic C_2 spectra are given for the three carbon abundances, $\log \epsilon(C) = 7.85 \pm 0.1$.

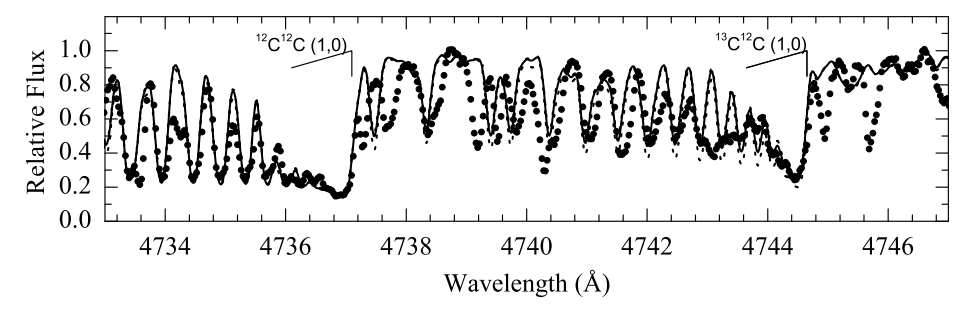


Fig. 10. The observed spectrum of HD 209621 in the wavelength range around the Swan system (1,0) band head. The C_2 synthetic spectra are given for the abundance of ^{12}C , $\log \epsilon(C) = 7.85$ and the three values of the ratio $^{12}C/^{13}C = 8$, 17 and 20.

of aluminum is found, [Al/Fe] = +0.5. Another Al I line at 3961.5 Å is affected by a prominent line of singly-ionized calcium at 3968.5 Å, and the use of this line for the abundance analysis was problematic. According to Andrievsky et al. (2008) the NLTE correction for aluminum could be as large as 0.4 dex.

Four relatively clean lines of ScII were selected, and the mean abundance

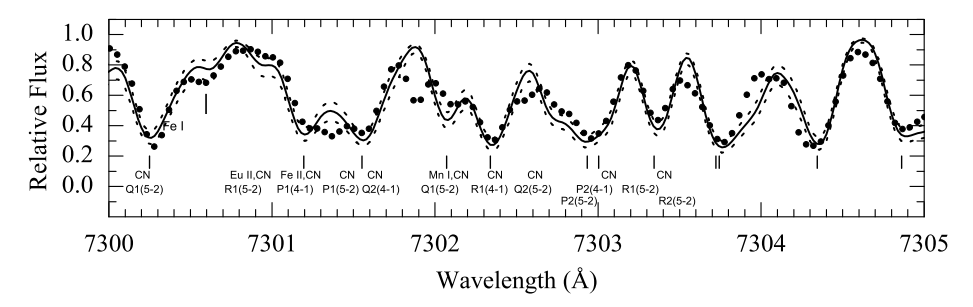


Fig. 11. The observed spectrum of HD 209621 in the wavelength range dominated by the CN Red system lines. The three synthetic CN spectra are given for the carbon abundance $\log \epsilon(C) = 7.85$, and for the nitrogen abundances $\log \epsilon(N) = 8.00 \pm 0.3$.

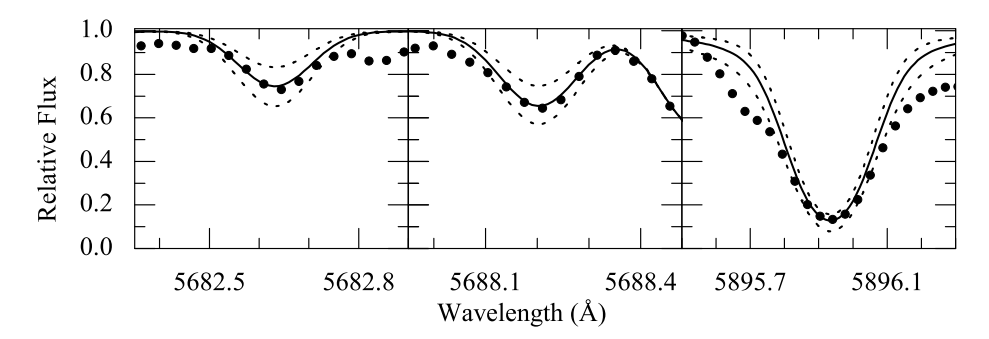


Fig. 12. Na I lines in the spectrum of HD 209621. The synthetic spectra are given for the sodium abundance $\log \epsilon(\mathrm{Na}) = 4.90 \pm 0.3$.

from equivalent widths was found to be $\log \epsilon(Sc) = 1.88$. Hyperfine structure (HFS) data for the selected lines was obtained from the Kurucz website⁴ (hereafter referred to as KLL). Spectral synthesis of the two profiles at 5657.9 and 5684.2 Å using the derived abundance shows a good fit with the observed profiles.

3.4.4. α -elements Mg, Si, Ca and Ti

Two strong Mg I lines at 5172.7 and 5183.6 Å are used to calculate the abundance of magnesium. Both lines are slightly blended in wings and are too strong (EW > 300 mÅ) for fine analysis using the method of atmospheric models. The third magnesium line at 5167.3 Å is partly blended with a Fe I line of similar intensity. Spectral synthesis of the selected lines using the final abundances (Table 3) and $\log \epsilon(\text{Mg}) = 5.77$ shows a reasonable fit for all the magnesium lines (Figure 13). According to Merle et al. (2011), the NLTE correction for the Mg I 5183.6 Å line should not exceed 0.25 dex for the atmospheric parameter values of HD 209621.

Several Si I lines at 5684.5, 6131.6, 6131.8, 6142.5 and 6155.7 Å were selected for the abundance analysis of silicon. Unfortunately, most of these lines are blended with CN lines. Spectral synthesis of the little blended line at 6142.5 Å provides the silicon abundance $\log \epsilon(\mathrm{Si}) = 5.98$ or $[\mathrm{Si}/\mathrm{Fe}] = 0.38$.

⁴ http://kurucz.harvard.edu/linelists.html

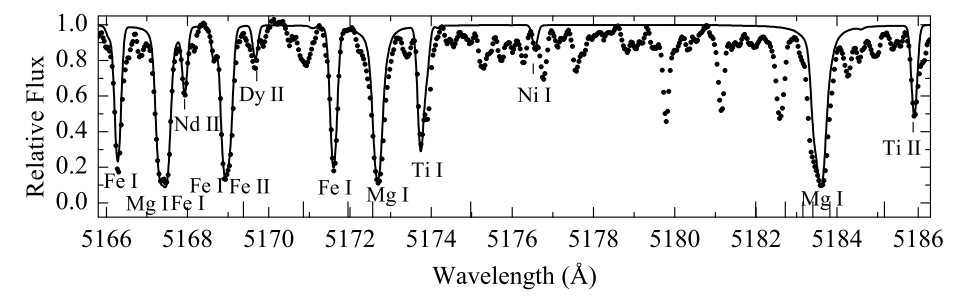


Fig. 13. The observed spectrum of HD 209621 around the magnesium triplet. Important atomic lines are identified, and the synthetic spectrum is given for the final abundances of iron peak elements and the magnesium abundance $\log \epsilon(Mg) = 5.77$.

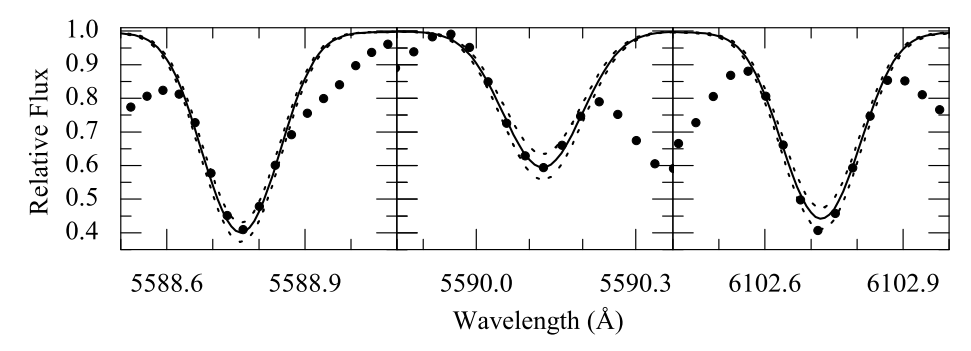


Fig. 14. Three Ca I lines in the spectrum of HD 209621. The synthetic profiles are given for the calcium abundance $\log \epsilon(\text{Ca}) = 4.94 \pm 0.15$.

Seven clean CaI lines were selected and abundance calculations on the basis of equivalent widths give the mean calcium abundance $\log \epsilon(\mathrm{Ca}) = 4.94 \pm 0.14$. Spectral synthesis of the selected profiles supports such calcium abundance (Figure 14). Regarding NLTE corrections, Mashonkina et al. (2007) have concluded, that at $[\mathrm{Ca/H}] \geq 2$ the NLTE abundance corrections of individual lines should be small due to different influence of the NLTE effects on the line wings and on the line core

The abundance of titanium from equivalent widths of ten Ti I lines and four Ti II lines is about $\log \epsilon(\text{Ti}) = 3.44$. Spectral synthesis of the selected titanium lines shows a slightly higher abundance of titanium, $\log \epsilon(\text{Ti}) = 3.54$ (see Figures 1 and 13).

3.4.5. Iron-peak elements

Twenty four unblended Fe I lines and ten Fe II lines give the mean iron abundance $\log \epsilon(\text{Fe}) = 5.59$. Spectral synthesis of selected iron lines in some spectral regions (see Figures 1, 4 and 13) supports this iron abundance. [Fe/H] = -1.91 is in excellent agreement with the iron abundance calculated by Goswami & Aoki (2010).

Most of the selected vanadium lines are found to be significantly blended. The mean abundance, calculated on the basis of equivalent widths for two VI lines and one VII line is $\log \epsilon(V) = 2.22$. The HFS data for the two VI lines was

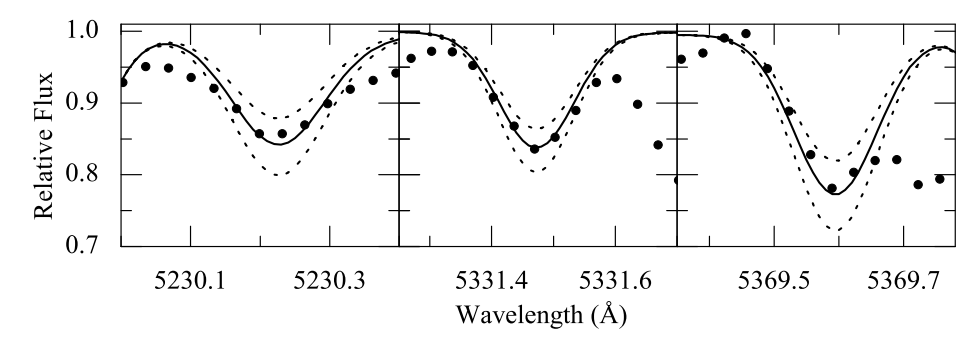


Fig. 15. Three Co I lines in the spectrum of HD 209621. The synthetic profiles are given for the cobalt abundance $\log \epsilon(\text{Co}) = 3.23 \pm 0.15$.

obtained from KLL. Spectral synthesis of the line at 6216.4 Å supports slightly lower abundance of vanadium, $\log \epsilon(V) = 2.17$ or [V/Fe] = -0.20. The abundance analysis of selected chromium lines on the basis of EWs leads to different values of chromium abundance calculated using the lines of neutral an ionized atoms. We conclude that all Cr II lines are blended. However, five Cr I lines, listed in Table 3, seem to be relatively clean and suitable for the abundance analysis. They give the chromium abundance $\log \epsilon(Cr) = 3.46$ or [Cr/Fe] = -0.27. According to Bergemann & Cesutti (2010), the NLTE Cr I-based abundances in metal-poor stars are systematically larger than that computed under the LTE approach by 0.2-0.4 dex.

Four lines of Mn I give the mean abundance of manganese $\log \epsilon(\mathrm{Mn}) = 3.43$. The HFS data for all lines was obtained from KLL. Three of these four lines are located fairly close to each other (4754.0, 4765.8 and 4766.4 Å), and the spectral synthesis of these lines supports the accepted abundance. Mn I lines are known to be affected by NLTE effects. From the results obtained by Bergemann & Gehren (2008) we conclude that the NLTE corrections for the Mn I lines at low metallicity and temperature can exceed 0.4 dex.

Most of the Co I lines used in the abundance analysis of cobalt are quite weak, with equivalent widths less than 30 mÅ. Calculations on the basis of EWs give $\log \epsilon(\text{Co}) = 3.41$. Spectral synthesis, including the HFS data from KLL, supports a lower abundance of cobalt, $\log \epsilon(\text{Co}) = 3.23$ (Figure 15).

Ni I lines in the spectrum of HD 209621 are of good quality in comparison to lines of other elements. Nickel abundance derived from the EWs of six lines was found to be $\log \epsilon(\mathrm{Ni}) = 4.33$ dex. Spectral syntesis confirms this value for the lines at 4756.5, 4866.3 and 4976.3 Å. The value of [Ni/Fe] is close to zero.

The abundance of copper was derived using spectral synthesis of the line at 5218.2 Å for which the HFS data were available from KLL. The copper abundance was found to be $\log \epsilon(\mathrm{Cu}) = 2.57$.

Zn I line at 4810.5 Å was used to determine the abundance of zinc. This line seems to be quite free from blends. Other line at 4722.2 Å is close to the head of the C_2 molecular band and is not usable. Synthesis of the first line yields the abundance for zinc of $\log \epsilon(Zn) = 3.01$. For metal-poor F, G and K stars Takeda et al. (2005) found that the NLTE correction is smaller than 0.1 dex for the 4810.5 Å line.

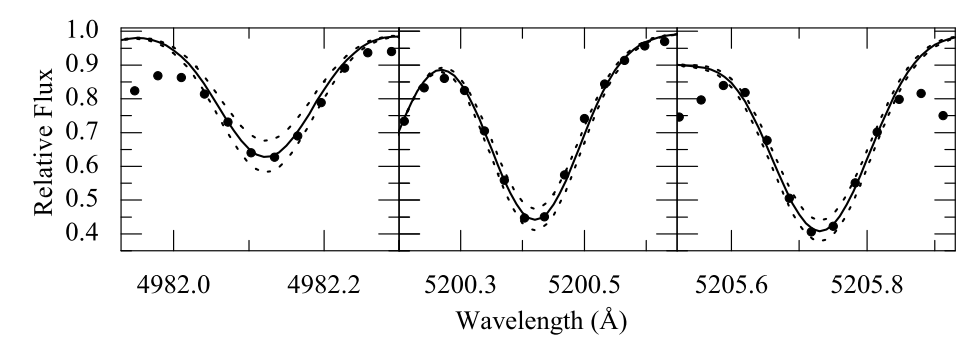


Fig. 16. Three Y II lines in the spectrum of HD 209621. The three synthetic profiles are given for the yttrium abundance $\log \epsilon(Y) = 1.07 \pm 0.15$.

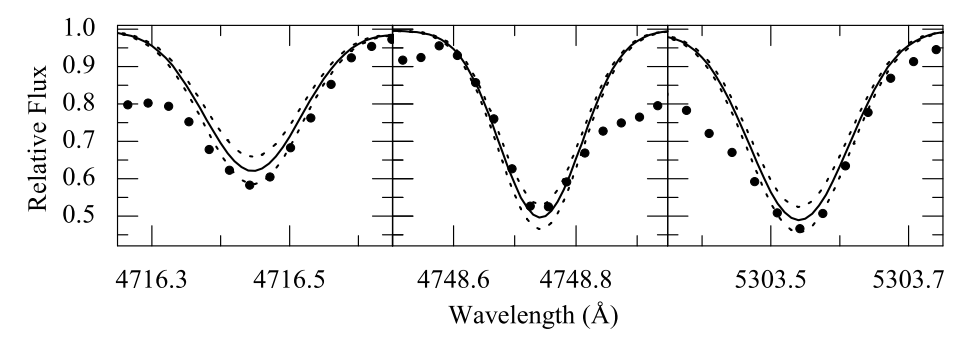


Fig. 17. La II lines in the spectrum of HD 209621. The three synthetic profiles are given for the lanthanum abundance $\log \epsilon(\text{La}) = 1.10 \pm 0.15$.

3.4.6. Neutron-capture elements

Five Sr I lines were selected to estimate the strontium abundance. Unfortunately, the average abundance gives enhancement of about 1.5 dex relative to the Sun, and the scatter of abundances from line to line is extremely high apparently because of undetected blends. Synthesis of the best profile at 4607.33 Å yields the abundance $\log \epsilon(\mathrm{Sr}) = 2.23$. According to Bergemann (2012), non-LTE effects for Sr I lines are large and can reach up to 0.5 dex at $\mathrm{Z} = -2$.

Four relatively clean Y II lines are selected. Calculations of the yttrium abundance on the basis of equivalent widths gives the mean abundance $\log \epsilon(Y) = 1.07 \pm 0.07$. Spectral synthesis of the three best profiles at 4982.1, 5200.4 and 5205.7 Å confirms this result (Figure 16). Y I lines seem to be too weak for measurement in the crowded spectrum of HD 209621.

We were not able to find clean lines of zirconium. Both neutral and singly-ionized lines display large line-to-line scatter of abundances, calculated from equivalent widths. Three of the best lines are given in Table 2. Synthesis of the Zr II line at 3999 Å provides a low zirconium abundance of $\log \epsilon(\mathrm{Zr}) = 1.19$, however, we were not able to reproduce any other zirconium lines with this abundance. Synthesis of the other two lines listed in Table 2 gives the zirconium abundance $\log \epsilon(\mathrm{Zr})$ from 1.6 to 2.0 dex. It seems that $\log \epsilon(\mathrm{Zr})$ around 1.8 dex is the upper abundance limit. As noted by Velichko et al. (2011), non-LTE correction for Zr II

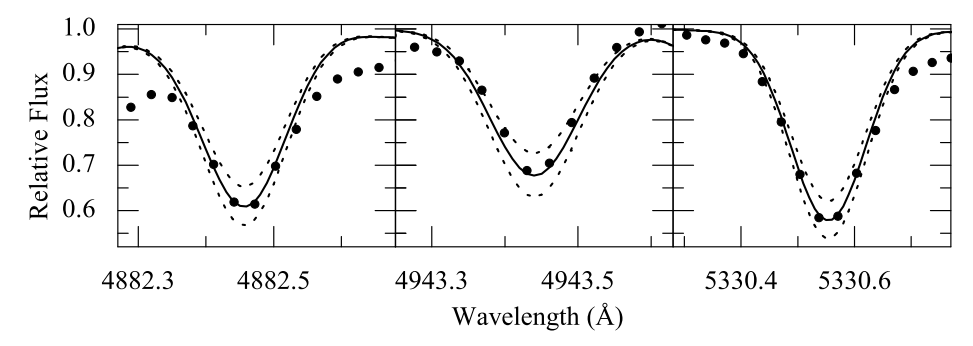


Fig. 18. Ce II lines in the spectrum of HD 209621. The synthetic profiles are given for the three cerium abundances $\log \epsilon(\text{Ce}) = 1.22 \pm 0.15$.

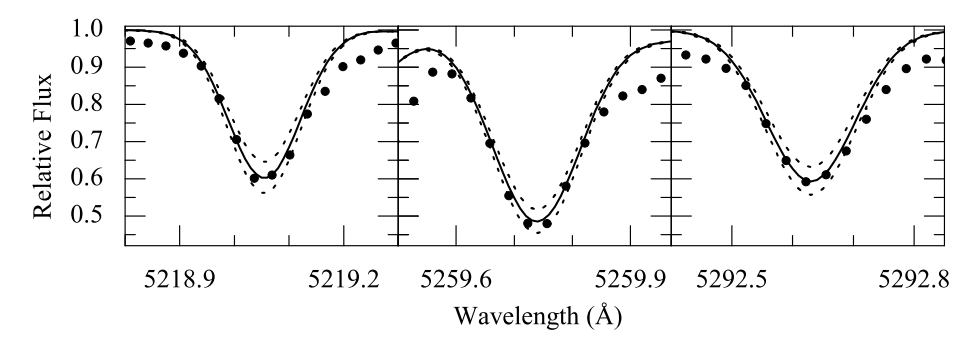


Fig. 19. Pr II lines in the spectrum of HD 209621. The synthetic spectra are given for the praseodymium abundance $\log \epsilon(\Pr) = 0.52 \pm 0.15$.

4050.33 Å line can be ~ 0.2 dex or larger.

The equivalent widths of four Ba II lines are measured and the abundance calculations from EWs give the mean barium abundance close to solar, $\log \epsilon(\mathrm{Ba}) = 2.10 \pm 0.18$. The spectral synthesis of the profile at 6141.7 Å supports such abundance. The HFS is neglegible for the Ba II subordinate lines at 5853.67 and 6496.93 Å (Mashonkina & Zhao 2005), and therefore was not considered in our calculations. According to Andrievsky et al. (2009) Ba II lines at 5853.67 and 6496.93 Å should have NLTE corrections smaller than ~ 0.1 dex for HD 209621.

Three relatively unblended lines of La II at 4716.4, 4748.7 and 5303.5 Å are selected. Abundances calculated from equivalent widths provide the mean lanthanum abundance $\log \epsilon(\text{La}) = 1.20$ dex. Spectral synthesis of these lines gives slightly lower abundance, 1.10 ± 0.20 dex (Figure 17).

The mean abundance calculated from equivalent widths of eight Ce II lines is $\log \epsilon(\text{Ce}) = 1.07 \pm 0.13$. Spectral synthesis of the three best profiles gives slightly higher abundance for cerium, $\log \epsilon(\text{Ce}) = 1.22$ (Figure 18).

For the abundance analysis four Pr II lines, less affected by molecular lines, are selected between 5200–5300 Å. A solar abundance was found from equivalent widths. Spectral synthesis of the three best lines gives slightly lower abundance of praseodymium, $\log \epsilon(\text{Pr}) = 0.52 \pm 0.06$ (Figure 19).

Twelve singly-ionized unblended lines are selected for the abundance analysis

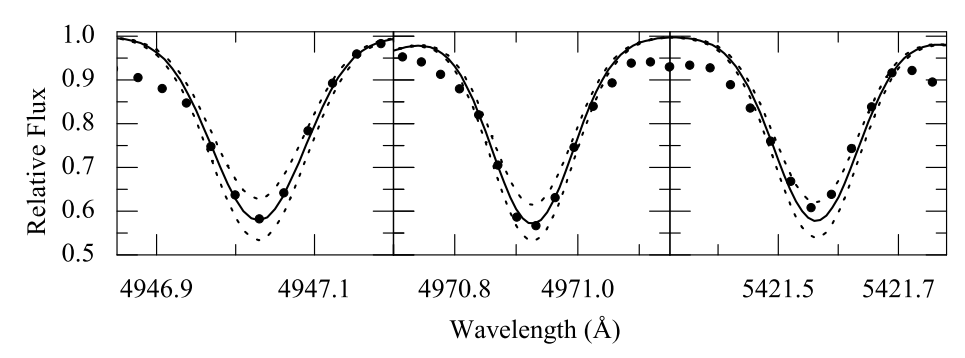


Fig. 20. Nd II lines in the spectrum of HD 209621. The synthetic profiles are given for the three neodymium abundances, $\log \epsilon(\mathrm{Nd}) = 1.11 \pm 0.15$.

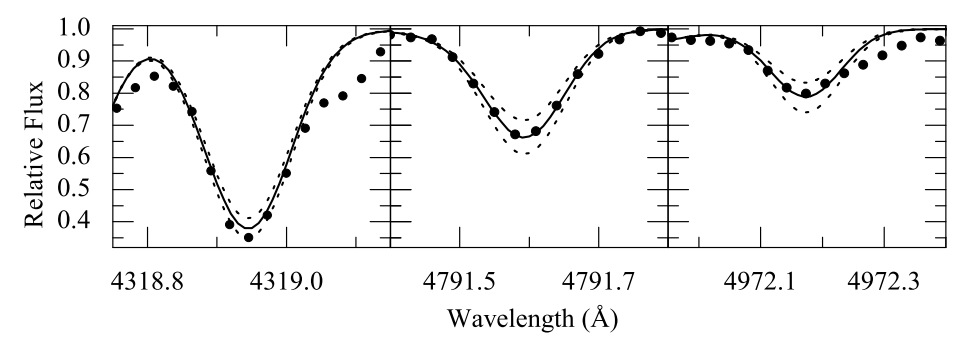


Fig. 21. Sm II lines in the spectrum of HD 209621. The synthetic spectra are given for the samarium abundance $\log \epsilon(\mathrm{Sm}) = 0.56 \pm 0.15$.

of neodymium. The mean abundance was found to be $\log \epsilon(\mathrm{Nd}) = 1.11 \pm 0.12$ from equivalent widths. Synthesis of the three selected lines supports this value (Figure 20).

Five unblended lines of samarium are selected. Spectral synthesis of the three best profiles at 4318.9, 4791.6 and 4972 Å gives the abundance of samarium $\log \epsilon(\mathrm{Sm}) = 0.56 \pm 0.11$ (Figure 21).

Spectral synthesis of the three Gd II lines at 4037.3, 4037.8 and 4478.8 Å gives the abundance $\log \epsilon(\mathrm{Gd}) = 0.70 \pm 0.12$.

Two Dy II lines at 3983.7 and 3996.7 Å are selected for the abundance analysis. Equivalent widths give almost identical abundance for both lines, $\log \epsilon(\mathrm{Dy}) = 0.60$. Such abundance is well reproduced by spectral synthesis of the line at 3983.7 Å.

Spectral synthesis of Yb II line at 3988 Å gives the abundance of ytterbium $\log \epsilon(\mathrm{Yb}) = 0.49$.

The abundance of europium is derived using the Eu II line at 6437.6 Å. The line is blended by a CN line on the right wing. Spectral synthesis, including the HFS data from KLL, gives the abundance $\log \epsilon(\text{Eu}) = 0.16$ (Figure 22) using the oscillator strength $\log gf = -0.320$. Other spectral lines of europium are significantly blended.

Table 3. The mean absolute and relative abundances in the atmosphere of HD 209621 calculated using $T_{\rm eff} = 4400$ K, $\log g = 1.0$ (cgs), and $\xi_{\rm t} = 1.9$ km s⁻¹.

Species	Z	$\log \epsilon(X)_{\odot}$	$\log \epsilon(X)^a$	σ^b	n^c	[X/H]	[X/Fe]	$[X/Fe]^d$	$[X/Fe]^e$
Li I	3	1.05	1.2^{s}	0.24	_	+0.15	_	_	_
$^{\mathrm{C}}$	6	8.43	7.85^{s}	0.10	_	-0.58	+1.33	+1.25	+2.29
N	7	7.83	8.00^{s}	0.30	_	+0.17	+2.08	_	_
ΟI	8	8.69	7.54^{s}	0.24	1	-1.15	+0.76	_	_
NaI	11	6.24	4.90	0.08	4	-1.34	+0.57	+0.02	_
MgI	12	7.60	5.77^{s}	0.12	2	-1.83	+0.08	+0.17	_
AlI	13	6.45	5.04^{s}	0.24	1	-1.41	+0.50	_	_
SiI	14	7.51	5.98^{s}	0.24	1	-1.53	+0.38	_	_
CaI	20	6.34	4.94	0.14	7	-1.40	+0.51	+0.08	_
$\operatorname{Sc}\operatorname{II}$	21	3.15	1.88	0.09	4	-1.27	+0.64	+0.72	_
Ti I	22	4.95	3.40	0.11	10	-1.55	+0.36	_	_
${ m TiII}$	22	4.95	3.48	0.03	4	-1.47	+0.44	+0.72	_
Ti	22	4.95	3.54^{s}	0.10	10	-1.41	+0.50	_	_
VI	23	3.93	2.22^{s}	0.12	2	-1.71	-0.20	_	_
$\operatorname{Cr} \operatorname{I}$	24	5.64	3.46^{s}	0.12	5	-2.18	-0.27	-0.20	_
$\operatorname{Mn} I$	25	5.43	3.43	0.08	4	-2.00	-0.09	_	_
$\operatorname{Fe} \operatorname{I}$	26	7.50	5.57	0.10	24	-1.93	_	_	_
${ m FeII}$	26	7.50	5.61	0.10	10	-1.89	_	_	_
CoI	27	4.99	3.23^{s}	0.14	6	-1.76	+0.15	_	_
Ni I	28	6.22	4.33	0.06	6	-1.89	+0.02	-0.01	_
Cu I	29	4.19	2.57^{s}	0.24	1	-1.62	+0.29	_	_
$\operatorname{Zn} \operatorname{I}$	30	4.56	3.01	0.24	1	-1.55	+0.36	+0.24	_
$\operatorname{Sr} \operatorname{I}$	38	2.87	2.23^{s}	0.24	1	-0.64	+1.27	+1.02	$+1.1\pm0.3$
YII	39	2.21	1.07	0.07	4	-1.14	+0.77	+0.36	_
${ m Zr}{ m I}$	40	2.58	1.86^{s}	0.24	2	-0.72	+1.19	+1.80	_
${ m ZrII}$	40	2.58	1.19^{s}	0.24	1	-1.39	+0.52	_	_
BaII	56	2.18	2.10	0.18	4	-0.08	+1.83	+1.70	_
LaII	57	1.10	1.10^{s}	0.20	3	0.00	+1.91	+2.41	_
$\mathrm{Ce}\mathrm{II}$	58	1.58	1.22^{s}	0.13	8	-0.36	+1.55	+2.04	$+2.8\pm0.3$
$\Pr{ ext{II}}$	59	0.72	0.52^{s}	0.06	4	-0.20	+1.71	+2.16	$+2.2 \pm 0.7$
NdII	60	1.42	1.12	0.12	13	-0.30	+1.61	+1.87	$+2.4\pm0.6$
$\mathrm{Sm}\mathrm{II}$	62	0.96	0.56^{s}	0.11	5	-0.40	+1.51	+1.46	_
Eu II	63	0.52	0.16	0.24	1	-0.36	+1.55	+1.35	_
$\operatorname{Gd} \operatorname{II}$	64	1.07	0.70^{s}	0.12	3	-0.37	+1.54	_	_
DyII	66	1.10	0.60	0.12	2	-0.50	+1.41	_	_
YbI	70	0.84	0.49^{s}	0.24	1	-0.35	+1.56	_	_

 $^{^{}a\ s}$ marks the abundances derived using spectral synthesis

3.4.7. Error estimates and confrontation with previous abundances

The random errors of the abundances are listed in Table 3. They are equal to the standard deviations of the abundances in the case of three and more lines. In the case of one line, the given random error was accepted to be two mean standard deviations. Systematic errors of the abundances, produced by uncertainties in the atmospheric parameters $T_{\rm eff}$ (± 100 K), $\log g$ (± 0.3 dex) and ξ_t (± 0.3 km s⁻¹), are listed in Table 4. The root-sum-squared (RSS) uncertainties are presented in the last column of Table 4. It is evident that the systematic abundance errors are smaller than about 0.2 dex for most of the elements. The individual abundances,

 $[^]b$ σ is the standard deviation of the abundance

 $^{^{}c}$ n is the number of spectral lines used for the abundance calculation

^d [X/Fe] values from Goswami & Aoki (2010)

^e [X/Fe] values from Vanture (1992b)

Table 4. Systematic errors in the abundances produced by the uncertainties in the atmospheric parameters.

Species	$\delta(T_{ m eff})$	$\delta(\log g)$	$\delta(\xi_{\rm t.})$	Δ
•	+100 K	+0.3	+0.3 km/s	dex
	0.40			
LiI	0.18	-0.03	-0.01	0.18
ΟI	0.00	0.11	0.00	0.11
NaI	0.14	-0.09	-0.05	0.17
MgI	0.16	-0.16	-0.04	0.23
AlI	0.08	-0.02	0.01	0.08
Si I	0.10	0.04	-0.06	0.12
$\operatorname{Ca} \operatorname{I}$	0.14	-0.07	-0.14	0.21
$\operatorname{Sc} \operatorname{II}$	0.00	0.09	-0.10	0.13
Ti	0.12	-0.08	-0.12	0.19
VI	0.18	-0.04	-0.10	0.21
$\operatorname{Cr} \operatorname{I}$	0.13	-0.05	-0.09	0.17
$\operatorname{Mn} \operatorname{I}$	0.18	-0.06	-0.08	0.21
${ m FeI}$	0.17	-0.05	-0.16	0.24
${ m FeII}$	-0.07	0.08	-0.14	0.18
CoI	0.10	-0.02	0.00	0.10
Ni I	0.14	0.00	-0.01	0.14
CuI	0.05	-0.02	-0.02	0.06
$\operatorname{Zn} \operatorname{I}$	-0.04	0.04	-0.10	0.11
$\operatorname{Sr} \operatorname{I}$	0.24	-0.08	-0.20	0.32
YII	0.02	0.08	-0.16	0.18
${ m Zr}{ m I}$	0.15	-0.03	-0.01	0.15
${ m ZrII}$	-0.01	0.02	-0.20	0.20
BaII	0.03	-0.06	-0.16	0.17
LaII	-0.05	0.08	-0.13	0.16
$\mathrm{Ce}\mathrm{II}$	0.00	0.09	-0.07	0.11
$\Pr{\mathrm{II}}$	0.00	0.08	-0.15	0.17
NdII	0.04	0.07	-0.20	0.22
$\mathrm{Sm}\mathrm{II}$	0.01	0.08	-0.03	0.09
EuII	-0.04	0.10	-0.03	0.11
$\operatorname{Gd} \operatorname{II}$	-0.01	0.07	-0.11	0.13
DyII	-0.02	0.03	-0.15	0.15
Ϋ́bΙ	0.13	0.00	-0.02	0.13

calculated for several unblended iron lines, give evidence that, in general, the continuum is defined correctly (Figure 23).

Vanture (1992a,b) and Goswami & Aoki (2010), using the same (standard) methods and similar atmospheric parameters, found abundances that differ for more than 10 times for most of the common elements, and the reasons of such discrepancy are not explained. The abundances calculated by Vanture (1992b) are in large excess, compared with our results (Figure 24). A logical explanation for such excesses can be the undetected molecular blends. Large standard deviations of the abundances provided by Vanture (1992) support such interpretation. Their resolution of $R=20\,000$ is evidently too low for the analysis of cool carbon stars, therefore most of the selected atomic lines are blended, and their equivalent widths are overestimated. Goswami & Aoki (2010) used a higher resolution, however, most of the abundances are still in excess in comparison with our results (Figure 24).

The real uncertainties are not known for the abundances calculated by Goswami & Aoki (2010), because they used only one line for most of the elements. The abundances of tungsten and erbium clearly are significantly overestimated because

of unknown blends. We have examined the spectral region around the line at 4057 Å, used by Goswami & Aoki (2010) to calculate the abundance of lead. It was a problem to calculate the synthetic spectrum in this region because of strong CH molecular lines. The line of Pb at 4057 Å is weak in comparison with the CH lines, and the uncertainty in the synthesis of such profile is quite large. For carbon-rich stars with the effective temperatures above 5000 K the situation is different, because the blending effects are much lower. A spectrum of very high resolution is needed to calculate mean abundances of light s-process elements and third peak neutron capture elements for HD 209621.

4. DISCUSSION AND CONCLUSIONS

Detailed analysis of a high-resolution spectrum of HD 209621 observed in a broad spectral region from 3650 to 7350 Å provides the atmospheric parameters $T_{\text{eff}} = 4400 \text{ K}, \log g = 1.0 \text{ (cgs)}$ and $\xi_t = 1.9 \text{ km s}^{-1}$. Low metallicity of the star with $[Fe/H] = 1.91 \pm 0.1$ is confirmed. Overabundance of carbon and the s-process elements is confirmed and the abundance pattern updated. The bolometric magnitude of HD 209621 is too low for AGB stars, therefore detected abundance anomalies, typical for late stages of stellar evolution, are apparently related to mass transfer from the companion star. The binary status for HD 209621 and a circularized orbit support the extrinsic

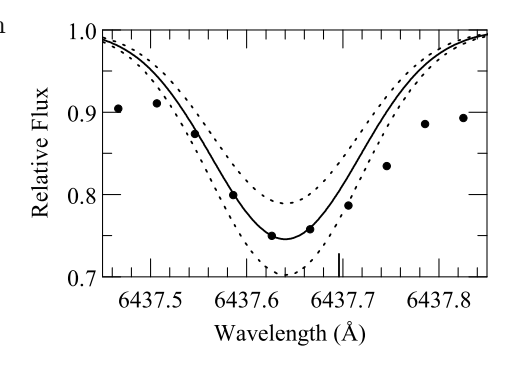


Fig. 22. Eu II line at 6437.6 Å in the spectrum of HD 209621. The synthetic spectra are given for the europium abundance $\log \epsilon(\mathrm{Eu}) = 0.16 \pm 0.15$. The vertical tick at 6437.696 Å is the position of CN line.

scenario of abundance anomalies and mass transfer. Substantial lithium depletion is in agreement with the theoretical prediction, based on surface convection and mass accretion from evolved star (see Charbonnel & Lagarde 2010 and references therein).

The abundances of 32 chemical elements in the atmosphere of HD 209621 were calculated using the methods of atmospheric models and spectral synthesis. The abundances for 11 elements are determined for the first time. Even at the high resolution, the spectrum was found to be extremely crowded, and the number of unblended atomic lines selected for abundance analysis was very limited. The overabundance of carbon and nitrogen at low effective temperature resulted in a large number of molecular lines produced by carbon bearing molecules (C₂, CN, etc.). We concluded that significant discrepancies in the calculated abundances of elements among different authors are mainly due to insufficient resolution and undetected blends. The available line lists and molecular data for carbon-bearing molecules are more uncertain and incomplete, in comparison with atomic data. Thus, fine quantitative analysis of abundances is difficult in the spectra of carbon-rich cool giants, and the abundance uncertainties are larger.

The abundance of oxygen was estimated for the first time using the forbidden line at 6300 Å. Oxygen was found to be enhanced, $[{\rm O/Fe}] \simeq +0.8\pm~0.2$, in agreement with the trend established for carbon-rich and metal-poor stars (see

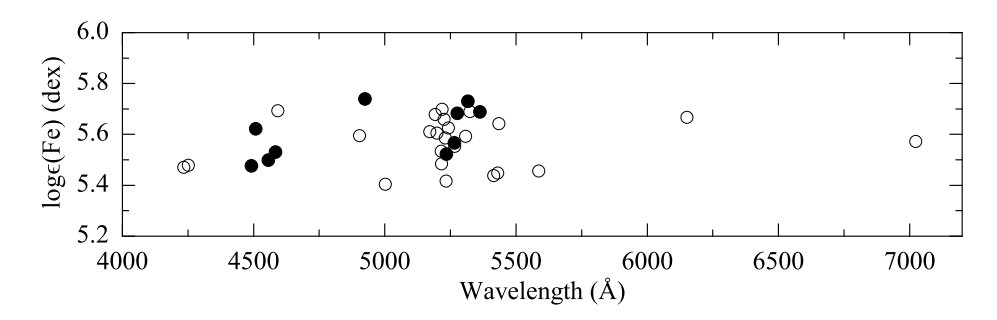


Fig. 23. The idividual abundances calculated for each Fe I (\circ) and Fe II (\bullet) line using the final atmospheric parameters.

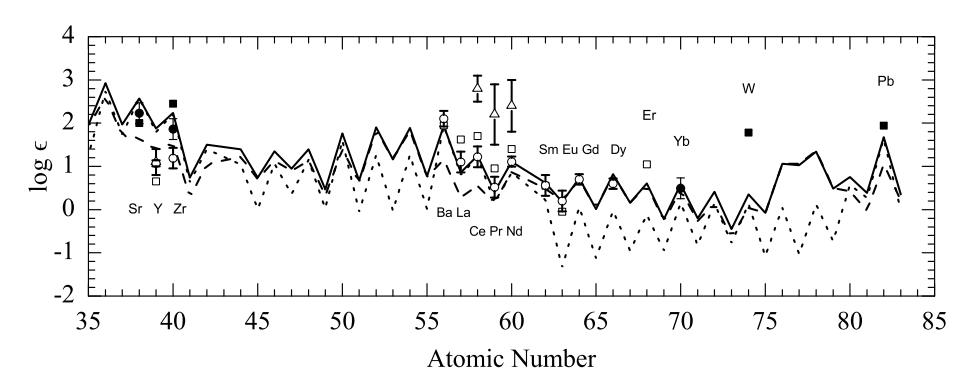


Fig. 24. The abundance pattern of neutron-capture elements in the atmosphere of HD 209621. The final mean abundances calculated using neutral (filled circles) and ionized (open circles) lines are given along with the scaled solar system abundance (solid line), solar s-process (dotted line) and r-process (dashed line) components according to Burris et al. (2000). The abundances derived by Vanture (1992b) and Goswami & Aoki (2010) are shown by triangles and squares.

Fig. 18 in Masseron et al. 2010). On the basis of rich molecular spectrum, the abundances of carbon and nitrogen are updated. The enhancement of carbon and nitrogen was confirmed, $[C/Fe] = +1.3 \pm 0.1$ and $[N/Fe] = +2.1 \pm 0.3$. The ratio of carbon isotopes was found to be low, $^{12}C/^{13}C = 17 \pm 5$. The status of a carbon star is confirmed by large carbon to oxygen ratio, $C/O \simeq 2.0$. The abundance of nitrogen was found to be very high. The low carbon to nitrogen ratio, $[C/N] \simeq -0.8$ and low $^{12}C/^{13}C$ ratio are in agreement with the theory of nucleosynthesis in AGB stars. According to Karakas & Lattanzio (2007), the nucleosynthesis in the 3–8 M_{\odot} AGB stars with Hot-Bottom-Burning leads to low [C/N] and low $^{12}C/^{13}C$ ratios (see Fig. 17 in Masseron et al. 2010). Thus, the abundances of CNO elements in the atmosphere of HD 209621 are in agreement with mass transfer scenario from former AGB intermediate-mass star to the companion (now red giant HD 209621) in the past.

The abundances for ten neutron capture elements are updated, and for three elements are calculated for the first time. Large discrepancies are found for some elements, probably because some abundances are calculated using only one line. The abundances for eight elements (Y, Ba, La, Ce, Pr, Nd, Sm, Gd) calculated in

this study, are based on three or more lines and provide representative and consistent distribution. The abundances for the rest neutron capture elements are determined using 1–2 lines and are of lower accuracy. The analyzed s-process elements are enhanced more than ten times comparing to the solar abundance. The heavy-to-light s-process element abundance ratio is found to be high, $[hs/ls] \simeq +0.6$. The abundance of almost pure r-process element europium based on one line is high, $[Eu/Fe] \simeq +1.5$. The high r-process abundance also supports gadolinium, $[Gd/Fe] \simeq +1.5$.

Figure 24 illustrates the abundance pattern of neutron-capture elements in the atmosphere of HD 209621. The abundances calculated by Vanture (1992b) and Goswami & Aoki (2010) are given for comparison purposes. As it is seen, some abundances calculated using the spectra of lower resolution, show higher enhancement relative to our data. Scaled solar system abundance adopted from Burris et al. (2000) was normalized to the mean abundance of neodymium calculated for 13 lines. The solar system s-process component was normalized to the cerium abundance (8 lines) and r-process component was normalized to Eu+Gd abundance (4 lines). As it is seen, the abundance pattern calculated in this study for elements with Z > 57 is reproduced well by the scaled solar system (s + r) abundances. The s-process component of the solar system does not fit the abundance pattern of HD 209621. The observed abundance pattern is more uncertain for the light s-process elements, because the abundance for strontium was calculated only for one line and the zirconium abundance calculated using the neutral lines and ions was found to be different. However, the yttrium abundance from four lines is more consistent with the solar r-process component. The barium to europium ratio calculated for HD 209621, $[Ba/Eu] \simeq +0.28$, is high and typical for carbon-enhanced metal-poor r/s stars. Thus, the abundances of HD 209621 meet the standards of CEMP-r/s subclass with [C/Fe] > +1.0 and 0.0 < [Ba/Eu] < +0.5(Beers & Christlieb 2005).

The abundances of nine Odd-Z elements, α -elements and iron-peak elements are updated, and for six elements the abundances are calculated for the first time. In general, the abundance pattern is typical for CEMP stars. The abundances of odd-Z elements Na, Al and Sc are moderately enhanced, $[\text{Odd-Z/Fe}] \simeq +0.5$ on average. The alpha elements Mg, Si, Ca and Ti are slightly enhanced too, $[\alpha/\text{Fe}] \simeq +0.4$. The abundances of iron-peak elements normalized to iron abundance are close to solar for the elements with at least three lines used. The abundance of chromium is underabundant, $[\text{Cr/Fe}] \simeq -0.3$, in agreement with the pattern found for the CEMP stars (see Aoki et al. 2007).

ACKNOWLEDGMENTS. This research has been financed by European Regional Development Fund (ESF grant No. 2010/0202/2DP/2.1.1.2.0/10/APIA/VIAA/013). The use of the WALD database operating at the Institute for Astronomy of the University of Vienna and the DREAM database operating at Mons University are acknowledged.

REFERENCES

Alonso A., Arribas S., Martínez-Roger C. 1999, A&AS, 140, 261 Andrievsky S. M., Spite M., Korotin S. A. et al. 2008, A&A, 481, 481 Andrievsky S. M., Spite M., Korotin S. A. et al. 2009, A&A, 494, 1083 Aoki W., Beers T. C., Christlieb N. et al. 2007, ApJ, 655, 492 Asplund M., Grevesse N., Sauval A. et al. 2009, ARA&A, 47, 481

Beers T. C., Christlieb N. 2005, ARA&A, 43, 531

Bergeat J., Knapik A., Rutily B. 2002, A&A, 390, 967

Bergemann M. 2012, in *The Chemical Evolution of the Milky Way*, eds. F. Matteucci & C. Morossi, available online at

http://www.sexten-cfa.eu/it/component/content/article/49

Bergemann M., Cescutti G. 2010, A&A, 522, 9

Bergemann M., Gehren T. 2008, A&A, 492, 823

Biémont E., Palmeri P., Quinet P. 1999, Ap&SS, 269, 635

Burris D. L., Pilachowski C. A., Armandroff T. E. et al. 2000, ApJ, 544, 302

Castelli F., Kurucz R. L. 2003, in *Modelling of Stellar Atmospheres*, eds. N. Piskunov, W. W. Weiss & D. F. Gray, ASP, IAU Symp., 210, A20

Charbonnel C., Lagarde N. 2010, A&A, 522, A10

Galazutdinov G. A. 1992, Special Astrophys. Obs. Preprint, 92, 2, available online at http://www.sao.ru/Doc-en/Science/Public/

Goswami A., Aoki W. 2010, MNRAS, 404, 253

Gray R. O., Corbally C. J. 1994, AJ, 107, 742

Han Z., Eggleton P. P., Podsiadlowski P. et al. 1995, MNRAS, 277, 1443

Karakas A., Lattanzio J. C. 2007, PASA, 24, 103

Keenan P. C., Morgan W. W. 1941, ApJ, 94, 501

Kupka F., Ryabchikova T. A., Piskunov N. E. at al. 2000, Baltic Astronomy, 9, 590

Mashonkina L., Korn A. J., Przybilla N. 2007, A&A, 461, 261

Mashonkina L., Zhao G. 2006, A&A, 456, 313

Masseron T., Johnson J. A., Plez B. et al. 2010, A&A, 509, A93

McClure R. D., Woodsworth A. W. 1990, ApJ, 352, 709

Meléndez J., Barbuy B. 2009, A&A, 497, 611

Merle T., Thévenin F., Pichon B., Bigot L. 2011, MNRAS, 418, 863

Munari U., Zwitter T. 1997, A&A, 318, 269

Perryman M. A. C., Lindegren L., Kovalevsky J. et al. 1997, A&A, 323, L49

Platais I., Pourbaix D., Jorissen A. et al. 2003, A&A, 397, 997

Prieto C. A., Lambert D. L., Asplund M. 2001, ApJ, 556, L63

Samus N. et al. 2011, General Catalogue of Variable Stars, vol. I–III

Sanford R. F. 1924, ApJ, 59, 339

Skrutskie M. F., Cutri R. M., Stiening R. et al. 2006, AJ, 131, 1163

Takeda Y., Hashimoto O., Taguchi H. et al. 2005, PASJ, 57, 751

Tsuji T., Iye M., Tomioka K. et al. 1991, A&A, 252, L1

Tsymbal V. 1996, in *Model Atmospheres and Stellar Synthesis*, eds. S. J. Adelman, F. Kupka, W. W. Weiss, ASP Conf. Ser., 108, 198

Vanture A. D. 1992a, AJ, 103, 2035

Vanture A. D. 1992b, AJ, 104, 1997

Velichko A. B., Mashonkina L. I., Nilsson H. 2010, Astronomy Letters, 36, 664

Wallerstein G. 1969, ApJ, 158, 607

Yamashita Y. 1975, PASJ, 27, 325

Zamora O., Abia C., Plez B. et al. 2009, A&A, 508, 909